crystals

MDPI

Article

Thermally Tunable Structural Color Based on Patterned Ultra-Thin Asymmetric Fabry–Perot Cavity with Phase-Change Material

Jiukai Fang, Shengnan Shi, Kaixiang Sun, Chengzhe Di, Yuwen Lin, Yeqing Zhu, Shan Zhang and Yanpeng Shi *

School of Microelectronics, Shandong University, Jinan 250100, China
* Correspondence: ypshi@sdu.edu.cn

Abstract: Tunable structural color has gained significant attention due to its dynamic characteristics. However, conventional devices are usually regulated only in their color capabilities by structural parameters, restricting real-time dynamic applications. In this study, we propose an ultra-thin asymmetric Fabry–Perot cavity patterned with phase-change materials (MPMP). The reversible phase transition of VO_2 induces changes in the MPMP's optical performance, enabling color mode switching through temperature control and resulting in rapid color conversion and low-temperature regulation. By adjusting relevant structural parameters of the VO_2 layer and nanodiscs, the color performance range can be tailored. Through numerical investigations, we demonstrate that MPMP can produce stable transformation of dynamic structural colors by harnessing the phase-change effect. Our research unveils new possibilities for applications such as anti-counterfeiting, bio/chemical sensing, and temperature sensing.

Keywords: dynamic structural color; metasurface; phase-change material; Fabry–Perot cavity; Mie resonance

check for updates

Citation: Fang, J.; Shi, S.; Sun, K.; Di, C.; Lin, Y.; Zhu, Y.; Zhang, S.; Shi, Y. Thermally Tunable Structural Color Based on Patterned Ultra-Thin Asymmetric Fabry–Perot Cavity with Phase-Change Material. *Crystals* **2023**, *13*, 996. https://doi.org/10.3390/cryst13070996

Academic Editor: Maxim V. Gorkunov

Received: 2 June 2023
Revised: 18 June 2023
Accepted: 19 June 2023
Published: 22 June 2023

Copyright: © 2023 by the authors. Licensee MDPI, Basel, Switzerland. This article is an open access article distributed under the terms and conditions of the Creative Commons Attribution (CC BY) license (https://creativecommons.org/licenses/by/4.0/).

1. Introduction

Color plays a crucial role in our lives [1]. According to the mechanisms of coloration, colors in nature can be mainly divided into pigment colors and structural colors [2,3]. The most common colors are generated by pigments, which form when chemical chromophores selectively absorb certain wavelengths of light [4]. Typically, pigment-based colors have a narrow color gamut, low resolution, and may lose their vibrancy under harsh conditions due to molecular degradation and potential environmental issues [5,6]. Structural color refers to colors produced by the interaction between light and the periodic micro- and nanoscale structures that overcome the obstacles of pigments [7]. Many methods to operate light through specific structures have been designed by researchers. Optical metasurfaces provide a new means to control light fields through resonances of their structures [8]. Metasurfaces can be composed of subwavelength structures made of metals [9–13] or dielectrics [14–16], and localized surface plasmon resonance (LSPR) and Mie resonance make it possible for metasurfaces to produce colors. Metasurfaces based on LSPR in metal nanocells can induce collective electron oscillations, making light scattering and absorption possible, and thereby achieving effective modulation of the amplitude, phase, and polarization of electromagnetic waves [9,17–19]. High refractive index dielectric and semiconductor structures can support Mie resonances with low optical loss, making it possible to expand the achievable color gamut and improve aspects of color quality, such as saturation and brightness [20–22].

Although the shape and geometric parameters of metasurface elements can have a significant control effect on color, they are difficult to change once manufactured. The fixed structure, with a determinate color space distribution, cannot adapt to changing

environments, and its static working mode limits broader applications such as stealth, dynamic full-color displays, optical anti-counterfeiting, and encryption. Therefore, the structure needs to be able to transition between two or even multiple chromatic states under external stimulation, forming a controllable dynamic structural color. Many methods have been studied to achieve dynamic structural color, such as color change induced by chemical reactions [23,24], force-induced color change [25,26], electrically induced color change [27–29], and phase-change material color change [30–34]. However, the reaction time of reversible electrochemical deposition operations is relatively long, slowing the refresh rate [23,24]. Dynamic structural color achieved through mechanical control, such as compression or stretching, lacks durability and stability. The color performance will significantly weaken after a period of compression or stretching [25,26]. Additionally, the device for electrically induced color change is relatively complex, and its production is more difficult [27–29].

Based on the circumstances mentioned above, it is crucial to develop a structural color that can be easily transformed and has a rapid response time. Phase-change materials (PCM) are capable of switching phases under external stimuli. During this phase change, the optical dielectric constant of the PCM changes correspondingly, causing a change in the device's reflection spectrum and resulting in a change in color. Research on structural colors based on PCM has made significant progress. The most commonly used PCMs are chalcogenide compounds, such as Ge2Sb2Te5 (GST) [35]. By utilizing the sharp change in optical properties caused by the phase transition between the crystalline and amorphous states under external stimuli, displays can be designed to exhibit significant changes in structural color before and after the phase transition [36,37]. However, chalcogenide compounds require thermal or electrical stimuli to achieve phase change at T = 150 °C. Although they can achieve a fast nanoscale phase change, the conditions required are relatively complex. In comparison, vanadium dioxide (VO_2) has a lower phase transition temperature (T = 68 °C) and a faster picosecond-level phase transition speed. VO_2 has been widely studied due to its excellent thermal stability and reversible phase transition states. It can achieve a reversible phase transition between an insulating state and a metallic state (IMT), corresponding to the monoclinic phase at low temperature and the rutile phase at high temperature. This results in a decrease in light density and a change in conductivity of three to four orders of magnitude [38]. Therefore, devices designed based on VO_2 can achieve high-speed and low-temperature control while producing certain optical property differences around the phase transition. Currently, research on VO_2 phase transition mainly covers the infrared band [39–41], for example, Barreda et al. propose the concept of quasi-bound states in the continuum (quasi-BIC) [42], and there is relatively little research on the visible light band [32,43]. Multilayer-based structural color is a common approach used to create color in various applications. One of the most common types of multilayer-based structural color is the Fabry–Perot (F–P) cavity, which contains the metal–insulator–metal (MIM) three-layer structure, such as the absorber Ag-VO_2-Al [32] or Ag nanoparticles-VO_2-Pt [43] three-layer MIM structure, and the VO_2-SiO_2-Ag [44] structure. This structure consists of two metallic mirrors separated by an optically transparent dielectric spacer, where the generation of structural colors is produced by the interference between multiple reflected light beams within the cavity. Research on infrared band optical solar reflectors has reported patterned VO_2 metasurface-SiO_2-Al [45] structures, which combine the advantages of thermochromism and plasmonic properties, achieving good selective reflection and absorption performance. However, currently, there are few reports on the design and application of VO_2-patterned structures in the visible light band.

In this study, we propose a patterned four-layer reflector structure (MPMP) based on PCM and an ultra-thin asymmetric Fabry–Perot cavity that can achieve stable color switching performance in the visible light spectrum through the combined effect of systematic Fabry–Perot resonance and Mie resonance. The VO_2 layer and VO_2 metasurfaces are crucial for controlling the color characteristics and color-changing properties of the system

before and after the phase transition. This paper focuses on the influence of VO_2 structural parameters on the system's color. Under the condition that all other structures remain unchanged, the system can cover most colors. By adjusting the thickness of the VO_2 layer and the radius of the VO_2 nanodisc, the hue, saturation, and brightness of the structural color can be fine-tuned. The nanodisc plays a crucial role in this fine-tuning, and the height of the VO_2 nanodisc can adjust only the brightness. Finally, by adjusting the VO_2-related parameters of the sample, we drew a reference color palette, which demonstrates the system's potential application value.

2. Materials and Methods

2.1. Metasurface Structure

The unit cell of the proposed MPMP structure under study is illustrated in Figure 1a, which shows the conversion of structural color under temperature control. Additionally, Figure 1b,c shows the schematic of the MPMP and its geometrical parameters. This is composed of a VO_2 nanodisc positioned on top and an ultra-compact asymmetric FP nanocavity at the bottom, with a phase-change material VO_2 film sandwiched between a top Ag film and a bottom Al film seated on the substrate. We selected Al as the bottom-layer material due to its high reflectivity across all visible wavelengths and chose Ag for its low absorption loss and high reflectivity [46]. The substrate can be either a rigid substrate (such as silicon or glass) or a flexible substrate (such as aluminum foil). The thickness of each layer is defined as h_1, h_2, h_3, h_4. Furthermore, the top VO_2 nanodisc is a periodic structure, and the radius and period of the nanodisc are denoted as r and p, respectively.

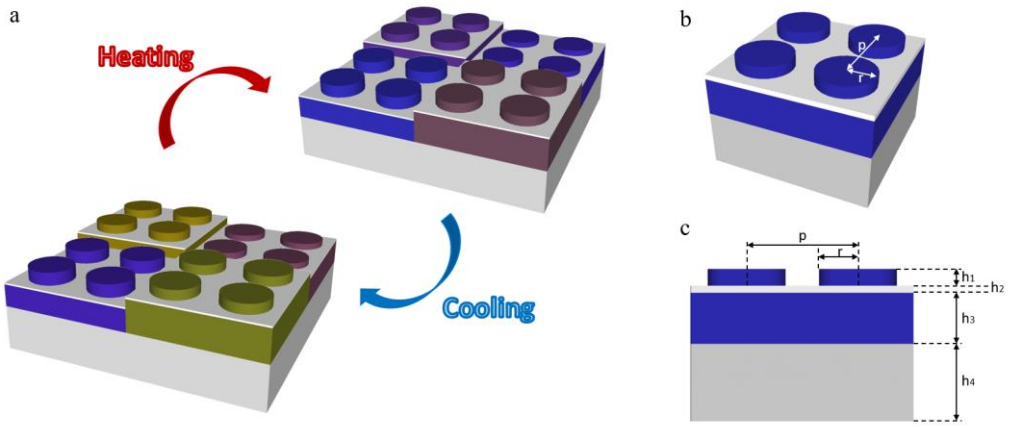


Figure 1. Schematic diagram of the proposed MPMP structure. (**a**) The diagram illustrates the changes in structural color of the samples after heating or cooling. MPMP with varying structural sizes exhibit different color rendering modes, which can vary significantly or only slightly. (**b**) A three-dimensional schematic of the MPMP structure. (**c**) Cross profile shows the relevant parameters of the designed structure. The surface of the MPMP structure comprises VO_2 nanodiscs with a period of p and a radius of r. h_1, h_2, h_3 and h_4 are the height of the nanodisc, the thickness of the Ag layer, the thickness of the VO_2 layer and the thickness of the Al layer, respectively.

The bottom Al reflecting layer with a thickness (h_4) of 200 nm is made larger than the skin depth in order to block the transmission of the incident plane wave. The Ag layer is used as the top reflective mirror with a thickness (h_2) of 5 nm, thin enough to allow a portion of the incident plane wave to pass through it. The performance of the intelligent thermal control partly relies on the middle VO_2 layer, which plays a crucial role in interference resonance as an optical cavity. When the temperature is below the phase transition temperature, the optical permittivity of VO_2 is in the insulator VO_2 state. When the temperature is above the phase transition temperature, the optical permittivity transfers to the metal VO_2 state. The difference in the dielectric constant of VO_2 before and after the phase transition results in a change of the structural reflectance, which leads to the

change of the structural color. The F–P resonance dominated by the VO_2 layer plays a leading role in the phase change, while the VO_2 nanodisc on top plays an auxiliary role in the regulation, with a relatively small effect on regulation.

The MPMP structure was designed and optimized through simulations using the finite difference time domain (FDTD) solutions. This approach discretizes Maxwell's equations into difference equations for numerical computation. The dielectric functions of Al and Ag were obtained from Palik's handbook [47] and are available in Lumerical's default material database. The complex refractive index data, including the refractive index n and the extinction coefficient k, of VO_2 at low (22 °C) and high temperatures (100 °C) were adopted from a previous report [47–51]. We also obtained data for widely used materials, GST [52] and Sb_2Se_3 [53], within the visible light range for simulations, as shown in Figure 2a,b. We focused on the data represented by dashed lines for the three materials, taking into consideration the variations in material losses. Within the visible light range, for both states, VO_2 demonstrates a lower extinction coefficient compared with GST, indicating that VO_2 experiences lower losses than GST. When comparing VO_2 with Sb_2Se_3, in the amorphous state, VO_2 exhibits lower losses than Sb_2Se_3 below approximately 670 nm, with slightly higher losses above this threshold. In the crystalline state, VO_2 displays significantly lower losses than Sb_2Se_3 below approximately 760 nm, with slightly higher losses beyond this point. Overall, VO_2 exhibits lower losses in comparison with Sb_2Se_3. Consequently, when compared with GST and Sb_2Se_3, VO_2 showcases a notable advantage in terms of lower losses.

Simulations were carried out with perpendicular illumination of plane waves on a single unit cell. In all simulations, the size of the spatial grids in all dimensions was set to 1 nm. Periodic boundary conditions were used in the x and y directions to replicate the periodic structures, while perfectly matched layer conditions were applied in the z direction to absorb the propagating waves. The reflectance and the electric and magnetic field distributions of the MPMP were recorded using frequency-domain field and power monitors.

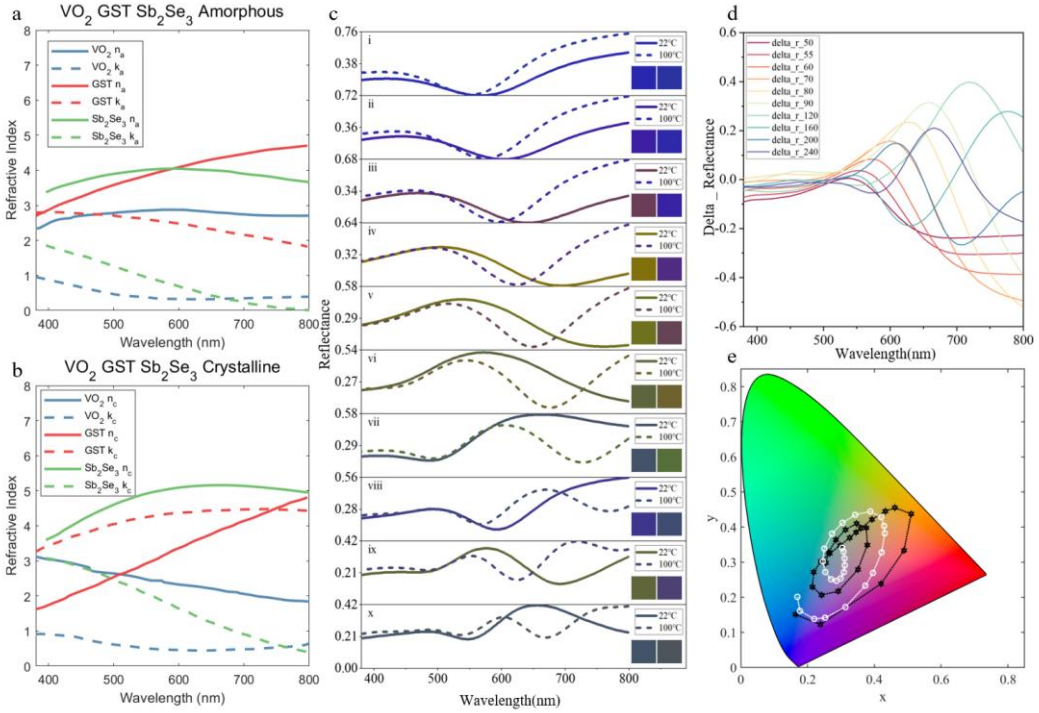


Figure 2. The data of material and the selected structures. (**a**) The refractive index of VO_2, GST and Sb_2Se_3 in the amorphous structure. (**b**) The refractive index of VO_2, GST and Sb_2Se_3 in the crystalline structure. (**c**) Ten samples were selected according to the structural color generated by MPMP. The

top VO_2 nanodisc radius (r) was fixed at 40 nm, the thickness (h_1) was 40 nm, the silver layer thickness (h_2) was 5 nm, and the bottom aluminum reflector thickness (h_4) was 100 nm. Only the thickness of the bottom VO_2 layer (h_3) was varied in order to observe the changes in the reflection spectrum and structural color before and after the phase transition. From top to bottom (i–x), the thickness of the VO_2 layer (h_3) was 50 nm, 55 nm, 60 nm, 70 nm, 80 nm, 90 nm, 120 nm, 160 nm, 200 nm, and 240 nm, respectively. (**d**) is defined as the difference between the reflection spectra of the monoclinic and rutile phases. The changes in the reflection spectra before and after the phase transition are shown. (**e**) For a set of samples in the color palette (with only the thickness of the bottom VO_2 layer (h_3) varying), the corresponding CIE 1931 chromaticity diagram is shown below, with a thickness variation of 5 nm for 50 nm–100 nm and a variation of 10 nm for 100 nm–250 nm.

2.2. Color Calculation

MATLAB was used to calculate color conversions from reflection spectra, based on previous color theory studies [3,52,54–56]. Once reflectance values were converted into color coordinates, the resulting colors could be visualized intuitively on the CIE1931 chromaticity diagram. The color coordinates were normalized XYZ tristimulus values, which are defined by a set of spectral reflectance factors. These reflectance factors, the relative energy of the illuminant, and the color-matching functions must be multiplied together at each wavelength and then summed. To obtain the tristimulus values, the simulated reflection data from the FDTD method were first interpolated to match the abridged set of color-matching functions, which were used at 5-nm intervals over the range of 380 nm to 800 nm. This range is the wavelength selection for this article and essentially covers the visible light spectrum. The tristimulus value can then be calculated using the following equations:

$$X = k \sum_{\lambda=380}^{\lambda=800} E(\lambda)\overline{x}(\lambda)P(\lambda)$$

$$Y = k \sum_{\lambda=380}^{\lambda=800} E(\lambda)\overline{y}(\lambda)P(\lambda)$$

$$Z = k \sum_{\lambda=380}^{\lambda=800} E(\lambda)\overline{z}(\lambda)P(\lambda)$$

Here, $E(\lambda)$ is the relative spectral power distribution of an illuminant, $\overline{x}(\lambda)$, $\overline{y}(\lambda)$ and $\overline{z}(\lambda)$ are the color-matching functions for the CIE1931 standard observers, $P(\lambda)$ is the spectral reflectance of the MPMP, and k is a normalized factor. The XYZ tristimulus values are normalized to a new scale ranging from 0 to 1, as follows:

$$x = \frac{X}{X+Y+Z}$$

$$y = \frac{Y}{X+Y+Z}$$

$$z = 1 - x - y$$

The resulting normalized values, which are the color coordinates, are denoted by x, y, and z. The resulting (x, y) plot represents the values of color on the CIE1931 chromaticity diagram. For this calculation, the light source condition used is D65, and the observation angle used is 2°.

2.3. Key Parameters of Color

Color is the sensation produced by the reflection of physical light from objects onto the optic nerve of the human eye. The perception of color by human eyes is determined by three primary characteristics: hue, chroma, and lightness. Hue is directly related to the frequency of the light wave, and refers to the different frequencies of color, with red having

the lowest frequency and purple the highest. Chroma is a numerical representation of the vividness of a color, calculated according to the degree of gray in the color. Saturation is another term for chroma. Lightness describes the brightness and darkness of a color, with lighter colors having a higher value and darker colors having a lower value. Together, these three characteristics give rise to the overall perception of color.

3. Results and Discussion

3.1. The Influence of Temperature on Structural Color

After undertaking the above analysis, we obtained the reflectance of the structure through simulation, which can be converted into corresponding colors. We present partial data selected from large-scale simulations in Figure 2c. The radius (r) of the nanodisc at the top of the structure is fixed at 40 nm, with a height (h_1) of 40 nm, and the thickness (h_3) of the VO_2 layer at the bottom of the structure adjusted. To better display the data transformation characteristics, we used a step size of 5 nm for the thickness (h_3) changing from 50 nm to 100 nm, and a step size of 10 nm for the thickness (h_3) changing from 100 nm to 250 nm. With the series of data obtained, we marked the corresponding colors on the color palette, as shown in Figure 2e. The sample of data in Figure 2c is derived from the selected sample shown in Figure 2e. We show the reflectance and the corresponding transformed colors in Figure 2c, with the thickness (h_3) of the VO_2 layer at the bottom being, successively, 50 nm, 55 nm, 60 nm, 70 nm, 80 nm, 90 nm, 120 nm, 160 nm, 200 nm, and 240 nm. In the figure, the solid line represents the data at low temperature (monoclinic phase), while the dashed line represents the data at high temperature (rutile phase), corresponding to the insulator VO_2 state and metal VO_2 state, respectively. As shown in Figure 2c, the left color panel corresponds to the reflectance at the monoclinic phase, while the right color panel corresponds to the rutile phase. The colors of the lines correspond to the structural colors. Furthermore, it can be observed that, with the increase of the thickness of the bottom VO_2 layer, the reflectance spectrum in both phases shows a trend of redshift, corresponding to a color transition that initiates from the short-wavelength blue range.

For VO_2 layer thicknesses less than 60 nm, as depicted in Figure 2(ci,cii), there is minimal variation around the phase transition, resulting in a uniform medium blue structural color. This can be attributed to the insufficient difference in the optical path created by the VO_2 layer at the bottom. However, as the thickness (h_3) increases to 60 nm, distinct colors corresponding to different states of VO_2 start to emerge. As shown in Figure 2(ciii), these colors are closer to maroon and royal blue, respectively, and exhibit relatively high saturation. At the same time, significant differences can be seen in the reflectance around the phase transition. Combined with Figure 2d, these differences are mainly reflected in the longer bands of visible light, and the positions of the reflectance valley and corresponding absorption peaks are different, as shown in Figure 2(civ,cv). When the thickness is increased further, the color difference around the phase transition is still obvious, but the color saturation decreases somewhat, as shown in Figure 2(cvi,cvii). When the thickness is too large, the difference in color still exists, but the overall reflectivity is low, resulting in an actual situation where the color is not easy to distinguish. At the same time, the relative size of reflectance corresponding to reflection peaks and valleys is further reduced, so the saturation and brightness of the corresponding color are low. The above factors lead to the structural color not having a good visual effect.

Based on the calculated reflectance spectra of MPMP, Figure 2d shows the corresponding CIE 1931 chromaticity diagram with points extracted from the color palette, ordered according to the magnitude of the thickness of the VO_2 layer. The black and white marks indicate data for VO_2 in the monoclinic and rutile phases, respectively. As the thickness of the VO_2 layer increases, the corresponding reflection spectra exhibit a certain pattern of change. As the thickness of VO_2 increases, the difference between the corresponding data points around the phase transition gradually increases first and then decreases, as reflected by the distance on the CIE 1931 chromaticity diagram. When the thickness is low, the movement of points on the chromaticity diagram is noticeable, and the color saturation

is high. However, as the thickness increases, the position of the points changes more slowly, and when the thickness exceeds 200 nm, the data points are densely distributed in the middle region with only slight changes, resulting in lower color saturation. The change in data starts from blue, and, except for the green with high saturation, the other colors can change to a color with higher saturation. From the edge to the center, there is a spiral change, where the change in the position of the point gradually becomes smaller, resulting in decreased saturation. This suggests that, when the thickness is large enough, the color tends to stabilize, but the visual effect is not ideal, consistent with the earlier conclusion.

ΔR is defined as the difference between the reflectance at the monoclinic phase and at the rutile phase in order to amplify the reflectance changes around the phase transition. Figure 2d demonstrates that there is little difference around the phase transition in the short-wavelength band. Where the reflection spectra are significantly different around the phase transition, there is a trend of long wavelength movement. The peak position of ΔR has a distinct redshift with the increasing thickness of VO_2, which plays a leading role in, and is the source of, the color difference between the monoclinic phase and the rutile phase.

3.2. Physical Mechanism Investigation

To elucidate the primary physical mechanism of the proposed structure, we examined the global or local distribution of the electric field intensity ($|E|^2$) and magnetic field intensity ($|H|^2$) for the sample consisting of 70 nm VO_2 nanodisc/10 nm Ag/70 nm VO_2/100 nm Al. As depicted in Figure 3a,b, the electric field intensity distribution diagram indicates that the energy is primarily concentrated in the VO_2 layer at the bottom of the structure, which suggests that the color filtering performance is mainly attributed to the Fabry–Perot resonance. Additionally, the electric field intensity is stronger in the monoclinic phase than in the rutile phase, which corresponds to the distinct states of VO_2.

To better visualize the energy distribution of the electric and magnetic fields within the top nanodisc, we present the magnetic field diagram in Figure 3c,d, revealing a magnetic dipole resonance with an amplified magnetic field that is primarily concentrated within the VO_2 nanodisc. In other words, the VO_2 nanodiscs act as Mie resonators, causing optical reflection at certain wavelengths through the excitation of magnetic dipole resonance, thereby modulating the reflection of the incident light in conjunction with Fabry–Perot resonance. The bar of the two magnetic field diagrams in the two phases was set to the same range; thus, it is evident that the VO_2 in the monoclinic phase has a stronger Mie resonance than that in the rutile phase, as demonstrated by the relative value of the amplified magnetic field.

We also analyzed the distribution of the horizontal electric field at the resonant wavelength before and after the phase transition, as illustrated in Figure 3e,f. It was observed that the electric field exhibits a slight concentration at the interface between Ag and SiO_2, which can be interpreted as a localized surface plasmon (LSP) associated with the silver nanodiscs [30]. Within the same range of values, the electric field intensity was found to be higher for the rutile phase than for the monoclinic phase, which is in accordance with the properties of VO_2.

3.3. The Influence of Parameters on Structural Color

As mentioned earlier, the thickness of the bottom VO_2 layer is the main factor affecting the reflectance spectrum of MPMP, and its effect and mechanism have been discussed. In addition, other structural parameters related to VO_2 also have a certain influence on the performance of MPMP, such as the radius (r) and height (h_1) of the top nanodisc of MPMP. The following will elaborate on the effects of these two structural parameters on the overall reflectance performance.

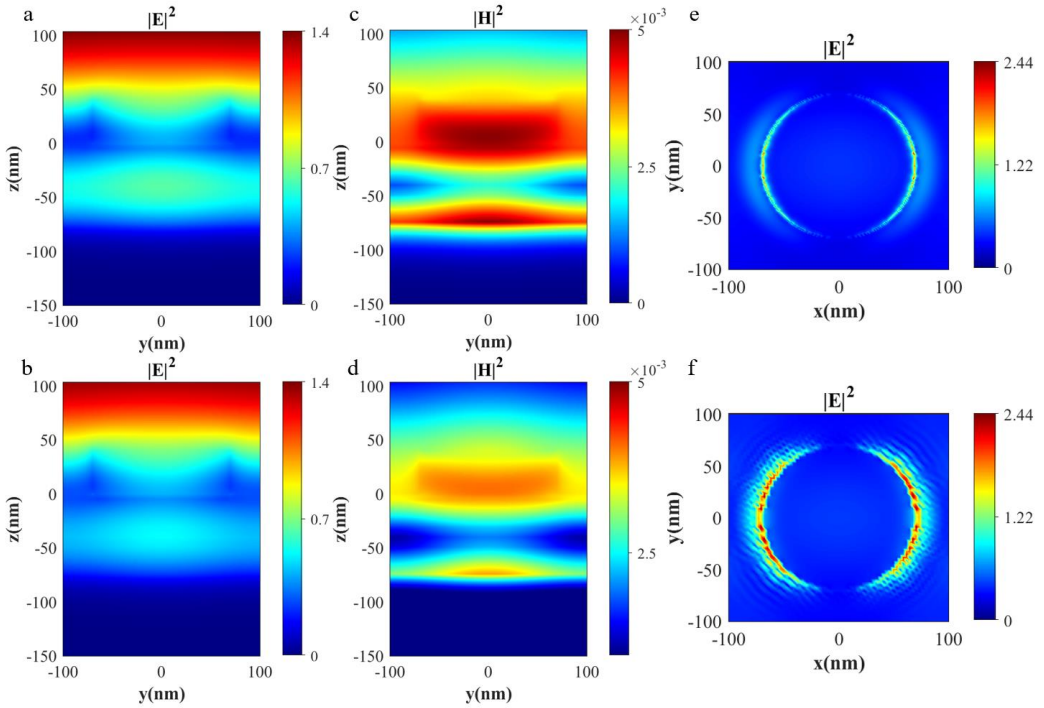


Figure 3. Cross-sectional distribution of the electromagnetic field in the y-z plane at the peak wavelength for the designed structure. The same numerical range is used for the electric field intensity distribution plots and the magnetic field intensity distribution plots, respectively, for different states, facilitating the comparison of the same field strength between different states. (**a**) The distribution of electric field strength in the y-z plane for the monoclinic phase. (**b**) The distribution of magnetic field strength in the y-z plane for the rutile phase. (**c**) The distribution of electric field strength in the y-z plane for the monoclinic phase. (**d**) The distribution of magnetic field strength in the y-z plane for the rutile phase. (**e**) The distribution of electric field strength in the x-y plane for the monoclinic phase. (**f**) The distribution of electric field strength in the x-y plane for the rutile phase.

Keeping the radius of the top VO_2 nanodiscs constant (r = 40 nm), as the thickness (h_1) of the nanodiscs increases we observe a gradual decrease in the overall refractive index and a slight redshift in the peaks and valleys of the reflectance curve. As shown in Figure 4a, except for a slight change in reflectance spectra when the disk thickness increases from 0 nm to 20 nm, there is little change in the position of the peaks and valleys of the reflectance spectrum as the thickness further increases, only a decrease in overall intensity. This is mainly because the absorption loss of the top VO_2 nanodiscs also increases with their thickness.

Because the structural color of the MPMP structure mainly depends on the position of the valleys, the adjustment of the nanodiscs has a very small effect on the position of the valleys, resulting in only slight color changes. However, due to the increase in nanodisc thickness (h_1), the overall reflectance decreases, leading to a slight decrease in the lightness and saturation of the color. Figure 4b shows the parameters of the structural color produced by MPMP before and after the phase transition, with hue, lightness, and saturation being normalized values obtained by calculation. It can be seen that, as the thickness of the nanodiscs increases, there is a slight shift in hue towards different colors and a slight decrease in lightness for both structures, and that the saturation of the monoclinic phase structure decreases slightly, while that of the rutile phase structure decreases more significantly. Therefore, the thickness of the nanodiscs can be used as a tool to fine-tune the lightness and saturation of the structural color.

As the radius of the nanodisc increases, the peak and valley wavelengths of the reflection spectrum demonstrate a redshift before and after the phase transition. When the VO_2 thickness at the bottom is lower (r = 60, 70 nm), as shown in Figure 5a,b, the peak

value initially decreases and then increases with increasing radius. However, as the bottom VO_2 thickness gradually increases, the trend of the peak value shifts to decreasing with increasing radius, as shown in Figure 5c,d. For structures with the same VO_2 thickness and phase state, the reflection spectra approximately intersect at a specific point. The reflectance at the wavelength corresponding to this point shows minimal variation with the radius of the nanodisc, indicating that it is independent of the structural parameters of the nanodisc. The position of this intersection point is influenced by the thickness of the bottom VO_2 layer, which acts as the Fabry–Perot resonance cavity. This suggests that, within a reasonable margin of error, its value equals the wavelength of the Fabry–Perot resonance. Figure 5a–d reveals that, as the VO_2 thickness increases, the fixed point moves towards longer wavelengths, resulting in a redshift phenomenon. This observation aligns with the conclusion regarding the resonance frequency of the Fabry–Perot resonance [31,32].

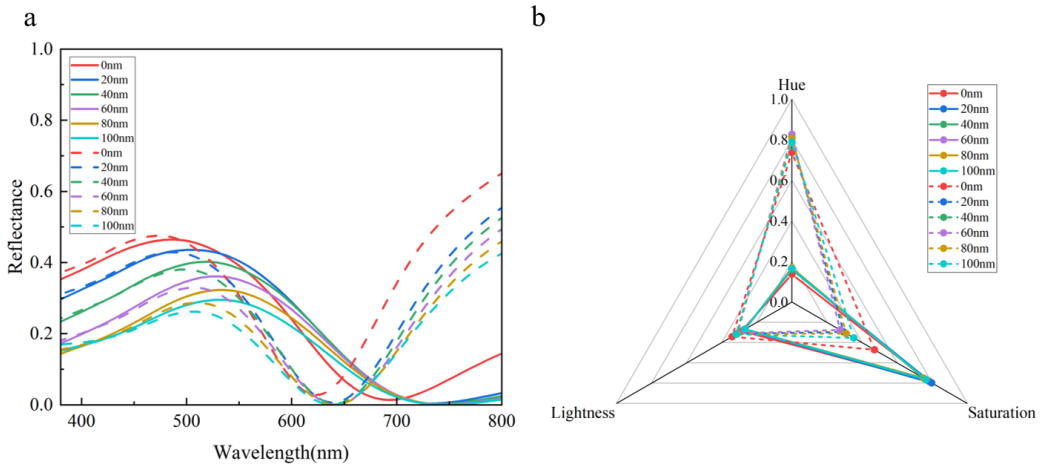


Figure 4. The effect of the thickness (h_1) of the top VO_2 nanodiscs on the structural color of MPMP. (**a**) Reflectance spectra of MPMP with top nanodiscs of thicknesses 0 nm, 20 nm, 40 nm, 60 nm, 80 nm, and 100 nm, with solid and dashed lines indicating data before and after the phase transition, respectively. (**b**) Normalized values of hue, lightness, and saturation, with solid lines indicating the structural color parameters of MPMP in the monoclinic phase and dashed lines indicating those in the rutile phase. Data with the same color represent unified structural parameters.

Based on the magnetic field distribution along the structure, it can be inferred that the top VO_2 nanodisc in the MPMP design acts as a Mie resonator, contributing to the structural color along with the Fabry–Perot resonance at the bottom. Additionally, due to the high extinction coefficient of VO_2, the nanodisc also plays a role in absorbing the incident light. These two effects together enable the top VO_2 nanodisc to finely tune the overall structural color. Considering the comprehensive impact of geometric parameters on MPMP, it becomes apparent that the modulation of VO_2 thickness has a more significant influence on its performance compared with the modulation of the top disk. This observation signifies the more pronounced role of Fabry–Perot resonance in the collective action of the Fabry–Perot and the Mie resonances. Furthermore, Figure 2c clearly demonstrates periodicity in the reflection curve, which aligns with the characteristic features of Fabry–Perot resonance. Hence, we can conclude that the coloration mechanism of MPMP encompasses a combination of Fabry–Perot resonance and Mie resonance, with Fabry–Perot resonance assuming a dominant role.

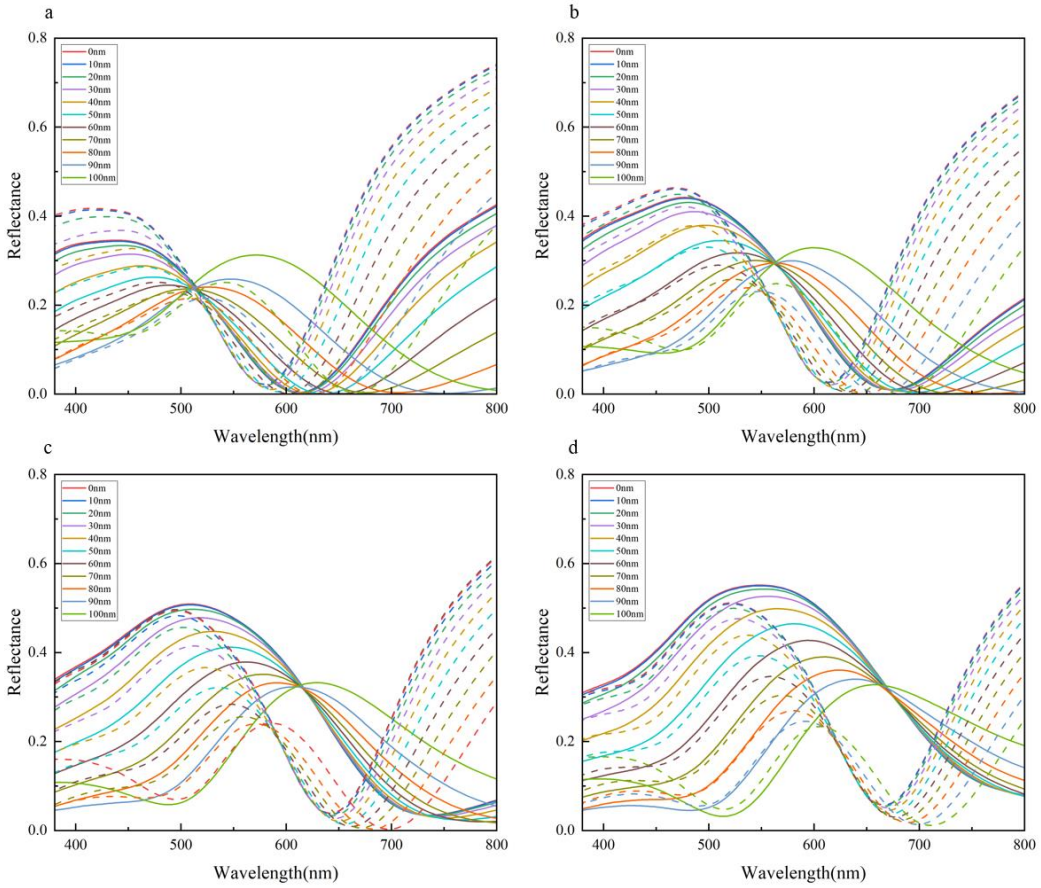


Figure 5. The influence of the top radius of the VO_2 nanodisc on the reflection spectra of MPMP is shown in four plots. The bottom VO_2 layer thicknesses are fixed at 60 nm, 70 nm, 80 nm, and 90 nm. The structure period is fixed at 200 nm, while the top radius is varied from 0 to 100 nm with a step of 10 nm. The solid and dashed lines represent the reflection spectra under the monoclinic and rutile phases, respectively. The same color is used for structures with the same radius but under different phases. (**a**) The reflection spectra of MPMP with a VO_2 thickness of 60 nm. (**b**) The reflection spectra of MPMP with a VO_2 thickness of 70 nm. (**c**) The reflection spectra of MPMP with a VO_2 thickness of 80 nm. (**d**) The reflection spectra of MPMP with a VO_2 thickness of 90 nm.

3.4. Practical Applications

The generation of dynamic structural colors is currently a research hotspot, as it can achieve a wide range of color patterns and can be intelligently controlled. As mentioned earlier, the color mode of MPMP can be switched by changing the heating temperature. As shown in Figure 6a,b, we demonstrate the color effects by only adjusting the VO_2 nanodiscs and the thickness of the bottom VO_2 layer. The depicted color distribution can serve as a valuable reference for practical applications in manufacturing. Each color block corresponds to the color converted from the sample data, and it can be observed that significant differences in color before and after the phase transition can be achieved within a certain size range, thereby achieving temperature-controlled dynamic structural colors. Meanwhile, we observed that, for a fixed radius, as the thickness increases, both MPMPs at two different temperatures exhibit a distinct periodicity. This finding aligns with our earlier observation that Fabry–Perot cavity resonance plays a dominant role in the phenomenon. In Figure 6c, the sample data of the color palette are marked on the CIE 1931 chromaticity diagram, and it can be seen that a large color coverage area can be achieved by controlling only VO_2, providing feasibility for practical applications.

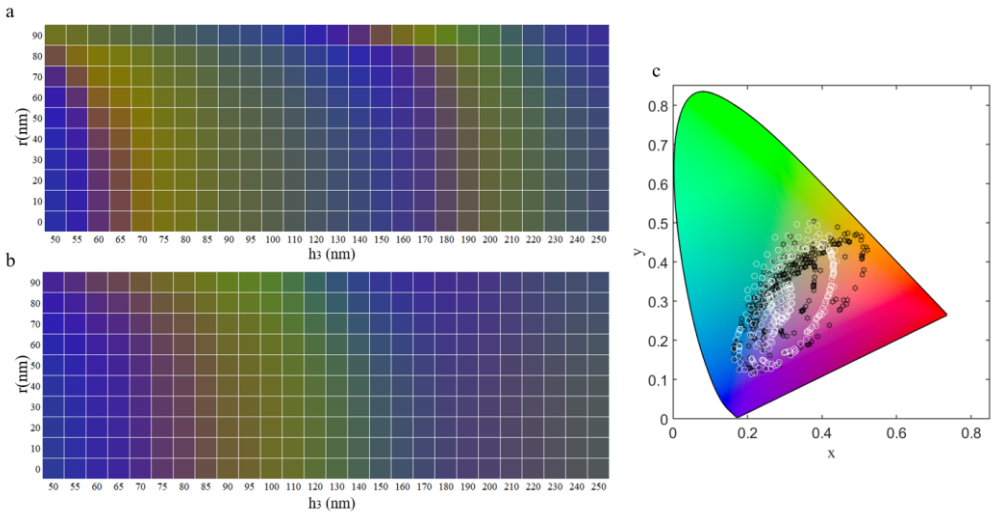


Figure 6. The demonstration of structural colors in MPMP. (**a**) The presentation of structural colors in the monoclinic phase with only VO_2-related parameters adjusted. (**b**) The presentation of the structural colors in the rutile phase with only VO_2-related parameters adjusted. (**c**) The corresponding CIE 1931 chromaticity diagram of the samples in the color palette before and after the phase transition. The thickness varies from 50 nm to 100 nm with a step size of 5 nm, and from 100 nm to 250 nm with a step size of 10 nm. The black hexagon represents the sample data at low temperature, and the white circle represents the sample data at high temperature.

4. Conclusions

In summary, our proposed dynamic structural color based on phase-change materials and an ultra-thin asymmetric Fabry–Perot cavity combined with a phase-change material metasurface demonstrates promising potential for a range of applications. By optimizing the VO_2-related parameters, we have shown that the thickness, radius, and height of the VO_2 layer and VO_2 nanodisc can regulate the hue, saturation, and brightness of the structural color. The combined effect of systematic Fabry–Perot resonance and Mie resonance allows for the generation of vivid and high-contrast structural colors. Furthermore, the phase-change characteristics of VO_2 enable the color of the system to be switched before and after the phase transition, enabling a wider range of applications, such as decoration, anti-counterfeiting, biosensing/chemical sensing, and temperature sensing. Overall, this study provides valuable insights into the development of dynamic structural color and its potential for practical applications.

Author Contributions: Conceptualization, J.F. and Y.S.; methodology, J.F. and Y.S.; software, J.F. and S.S.; validation, K.S., C.D. and Y.L.; formal analysis, J.F. and Y.Z.; investigation, J.F.; resources, Y.S.; data curation, J.F. and S.Z.; writing—original draft preparation, J.F.; writing—review and editing, J.F. and Y.S.; visualization, J.F.; supervision, J.F. and Y.S.; project administration, J.F.; funding acquisition, Y.S. All authors have read and agreed to the published version of the manuscript.

Funding: This work was supported by the National Natural Science Foundation of China under Grant 61805127, the Natural Science Foundation of Shandong Province under Grant ZR2019BF014, and the Fundamental Research Fund of Shandong University under Grant 2018TB002.

Data Availability Statement: The datasets are available from the corresponding author on reasonable request.

Conflicts of Interest: The authors declare no conflict of interest.

References

1. Vukusic, P.; Sambles, J.R. Photonic structures in biology. *Nature* **2003**, *424*, 852–855. [CrossRef] [PubMed]
2. Wu, Y.K.; Chen, Y.M.; Song, Q.H.; Xiao, S.M. Dynamic Structural Colors Based on All-Dielectric Mie Resonators. *Adv. Opt. Mater.* **2021**, *9*, 2002126. [CrossRef]

3. Srinivasarao, M. Nano-optics in the biological world: Beetles, butterflies, birds, and moths. *Chem. Rev.* **1999**, *99*, 1935–1961. [CrossRef] [PubMed]
4. Kulyk, O.; Rocard, L.; Maggini, L.; Bonifazi, D. Synthetic strategies tailoring colours in multichromophoric organic nanostructures. *Chem. Soc. Rev.* **2020**, *49*, 8400–8424. [CrossRef] [PubMed]
5. Rezaei, S.D.; Dong, Z.G.; Chan, J.Y.E.; Trisno, J.; Ng, R.J.H.; Ruan, Q.F.; Qiu, C.W.; Mortensen, N.A.; Yang, J.K.W. Nanophotonic Structural Colors. *ACS Photonics* **2021**, *8*, 18–33. [CrossRef]
6. Lundberg, I.; Milatou-Smith, R. Mortality and cancer incidence among Swedish paint industry workers with long-term exposure to organic solvents. *Scand. J. Work. Environ. Health* **1998**, *24*, 270–275. [CrossRef] [PubMed]
7. Fu, F.F.; Shang, L.R.; Chen, Z.Y.; Yu, Y.R.; Zhao, Y.J. Bioinspired living structural color hydrogels. *Sci. Robot.* **2018**, *3*, eaar8580. [CrossRef]
8. Glybovski, S.B.; Tretyakov, S.A.; Belov, P.A.; Kivshar, Y.S.; Simovski, C.R. Metasurfaces: From microwaves to visible. *Phys. Rep.* **2016**, *634*, 1–72. [CrossRef]
9. Cheng, F.; Gao, J.; Luk, T.S.; Yang, X.D. Structural color printing based on plasmonic metasurfaces of perfect light absorption. *Sci. Rep.* **2015**, *5*, 11045. [CrossRef]
10. Li, Z.G.; Wang, W.; Rosenmann, D.; Czaplewski, D.A.; Yang, X.D.; Gao, J. All-metal structural color printing based on aluminum plasmonic metasurfaces. *Opt. Express* **2016**, *24*, 20472–20480. [CrossRef]
11. Wang, Z.; Liang, Y.; Qu, J.; Chen, M.K.; Cui, M.; Cheng, Z.; Zhang, J.; Yao, J.; Chen, S.; Tsai, D.P.; et al. Plasmonic bound states in the continuum for unpolarized weak spatially coherent light. *Photonics Res.* **2023**, *11*, 260. [CrossRef]
12. Zheng, D.; Wen, Y.; Xu, X.; Lin, Y.-S. Metamaterial grating for colorimetric chemical sensing applications. *Mater. Today Phys.* **2023**, *33*, 101056. [CrossRef]
13. Cerjan, B.; Gerislioglu, B.; Link, S.; Nordlander, P.; Halas, N.J.; Griep, M.H. Towards scalable plasmonic Fano-resonant metasurfaces for colorimetric sensing. *Nanotechnology* **2022**, *33*, 405201. [CrossRef]
14. Sun, S.; Zhou, Z.X.; Zhang, C.; Gao, Y.S.; Duan, Z.H.; Xiao, S.M.; Song, Q.H. All-Dielectric Full-Color Printing with TiO_2 Metasurfaces. *ACS Nano* **2017**, *11*, 4445–4452. [CrossRef]
15. Yang, W.H.; Xiao, S.M.; Song, Q.H.; Liu, Y.L.; Wu, Y.K.; Wang, S.; Yu, J.; Han, J.C.; Tsai, D.P. All-dielectric metasurface for high-performance structural color. *Nat. Commun.* **2020**, *11*, 1864. [CrossRef]
16. Wang, L.; Wang, T.; Yan, R.Q.; Yue, X.Z.; Wang, H.M.; Wang, Y.D.; Zhang, J.Y. Tunable structural colors generated by hybrid Si_3N_4 and Al metasurfaces. *Opt. Express* **2022**, *30*, 7299–7307. [CrossRef] [PubMed]
17. Ellenbogen, T.; Seo, K.; Crozier, K.B. Chromatic Plasmonic Polarizers for Active Visible Color Filtering and Polarimetry. *Nano Lett.* **2012**, *12*, 1026–1031. [CrossRef] [PubMed]
18. Li, Y.L.; An, B.W.; Jiang, S.M.; Gao, J.; Chen, Y.L.; Pan, S.D. Plasmonic induced triple-band absorber for sensor application. *Opt. Express* **2015**, *23*, 17607–17612. [CrossRef]
19. Bai, Y.; Jiang, Y.Y.; Liu, L.H. Role of surface plasmon polaritons on the enhancement of the near-field thermal radiation from fishnet metamaterial. *J. Phys. D Appl. Phys.* **2014**, *47*, 445304. [CrossRef]
20. Kuznetsov, A.I.; Miroshnichenko, A.E.; Brongersma, M.L.; Kivshar, Y.S.; Luk'yanchuk, B. Optically resonant dielectric nanostructures. *Science* **2016**, *354*, aag2472. [CrossRef]
21. Moitra, P.; Slovick, B.A.; Li, W.; Kraychencko, I.I.; Briggs, D.P.; Krishnamurthy, S.; Valentine, J. Large-Scale All-Dielectric Metamaterial Perfect Reflectors. *ACS Photonics* **2015**, *2*, 692–698. [CrossRef]
22. Jahani, S.; Jacob, Z. All-dielectric metamaterials. *Nat. Nanotechnol.* **2016**, *11*, 23–36. [CrossRef] [PubMed]
23. Duan, X.Y.; Kamin, S.; Liu, N. Dynamic plasmonic colour display. *Nat. Commun.* **2017**, *8*, 14606. [CrossRef] [PubMed]
24. Chen, Y.Q.; Duan, X.Y.; Matuschek, M.; Zhou, Y.M.; Neubrech, F.; Duan, H.G.; Liu, N. Dynamic Color Displays Using Stepwise Cavity Resonators. *Nano Lett.* **2017**, *17*, 5555–5560. [CrossRef]
25. Seeboth, A.; Loetzsch, D.; Ruhmann, R. Piezochromic Polymer Materials Displaying Pressure Changes in Bar-Ranges. *Am. J. Mater. Sci.* **2012**, *1*, 139–142. [CrossRef]
26. Song, S.C.; Ma, X.L.; Pu, M.B.; Li, X.; Liu, K.P.; Gao, P.; Zhao, Z.Y.; Wang, Y.Q.; Wang, C.T.; Luo, X.G. Actively Tunable Structural Color Rendering with Tensile Substrate. *Adv. Opt. Mater.* **2017**, *5*, 1600829. [CrossRef]
27. Wang, G.P.; Chen, X.C.; Liu, S.; Wong, C.P.; Chu, S. Mechanical Chameleon through Dynamic Real Time-Plasmonic Tuning. *ACS Nano* **2016**, *10*, 1788–1794. [CrossRef]
28. Xu, T.; Walter, E.C.; Agrawal, A.; Bohn, C.; Velmurugan, J.; Zhu, W.Q.; Lezec, H.J.; Talin, A.A. High-contrast and fast electrochromic switching enabled by plasmonics. *Nat. Commun.* **2016**, *7*, 10479. [CrossRef]
29. Xiong, K.L.; Emilsson, G.; Maziz, A.; Yang, X.X.; Shao, L.; Jager, E.W.H.; Dahlin, A.B. Plasmonic Metasurfaces with Conjugated Polymers for Flexible Electronic Paper in Color. *Adv. Mater.* **2016**, *28*, 9956–9960. [CrossRef]
30. Shu, F.Z.; Yu, F.F.; Peng, R.W.; Zhu, Y.Y.; Xiong, B.; Fan, R.H.; Wang, Z.H.; Liu, Y.M.; Wang, M. Dynamic Plasmonic Color Generation Based on Phase Transition of Vanadium Dioxide. *Adv. Opt. Mater.* **2018**, *6*, 1700939. [CrossRef]
31. Zhao, J.C.; Zhou, Y.; Huo, Y.H.; Gao, B.; Ma, Y.G.; Yu, Y.T. Flexible dynamic structural color based on an ultrathin asymmetric Fabry–Perot cavity with phase-change material for temperature perception. *Opt. Express* **2021**, *29*, 23273–23281. [CrossRef] [PubMed]
32. He, J.Q.; Zhang, M.; Shu, S.W.; Yan, Y.; Wang, M.X. VO_2 based dynamic tunable absorber and its application in switchable control and real-time color display in the visible region. *Opt. Express* **2020**, *28*, 37590–37599. [CrossRef]

33. Rui, G.; Ding, C.; Gu, B.; Gan, Q.; Zhan, Q.; Cui, Y. Symmetric $Ge_2Sb_2Te_5$ based metamaterial absorber induced dynamic wide-gamut structural color. *J. Opt.* **2020**, *22*, 085003. [CrossRef]
34. He, Q.; Youngblood, N.; Cheng, Z.G.; Miao, X.S.; Bhaskaran, H. Dynamically tunable transmissive color filters using ultra-thin phase-change materials. *Opt. Express* **2020**, *28*, 39841–39849. [CrossRef]
35. Loke, D.; Lee, T.H.; Wang, W.J.; Shi, L.P.; Zhao, R.; Yeo, Y.C.; Chong, T.C.; Elliott, S.R. Breaking the Speed Limits of Phase-Change Memory. *Science* **2012**, *336*, 1566–1569. [CrossRef]
36. Rios, C.; Hosseini, P.; Taylor, R.A.; Bhaskaran, H. Color Depth Modulation and Resolution in Phase-Change Material Nanodisplays. *Adv. Mater.* **2016**, *28*, 4720–4726. [CrossRef] [PubMed]
37. Ding, F.; Yang, Y.Q.; Bozhevolnyi, S.I. Dynamic Metasurfaces Using Phase-Change Chalcogenides. *Adv. Opt. Mater.* **2019**, *7*, 1801709. [CrossRef]
38. Morin, F.J. Oxides Which Show a Metal-to-Insulator Transition at the Neel Temperature. *Phys. Rev. Lett.* **1959**, *3*, 34–36. [CrossRef]
39. Dicken, M.J.; Aydin, K.; Pryce, I.M.; Sweatlock, L.A.; Boyd, E.M.; Walavalkar, S.; Ma, J.; Atwater, H.A. Frequency tunable near-infrared metamaterials based on VO_2 phase transition. *Opt. Express* **2009**, *17*, 18330–18339. [CrossRef]
40. Savaliya, P.B.; Thomas, A.; Dua, R.; Dhawan, A. Tunable optical switching in the near-infrared spectral regime by employing plasmonic nanoantennas containing phase-change materials. *Opt. Express* **2017**, *25*, 23755–23772. [CrossRef]
41. Kats, M.A.; Blanchard, R.; Genevet, P.; Yang, Z.; Qazilbash, M.M.; Basov, D.N.; Ramanathan, S.; Capasso, F. Thermal tuning of mid-infrared plasmonic antenna arrays using a phase-change material. *Opt. Lett.* **2013**, *38*, 368–370. [CrossRef] [PubMed]
42. Barreda, A.; Zou, C.J.; Sinelnik, A.; Menshikov, E.; Sinev, I.; Pertsch, T.; Staude, I. Tuning and switching effects of quasi-BIC states combining phase-change materials with all-dielectric metasurfaces. *Opt. Mater. Express* **2022**, *12*, 3132–3142. [CrossRef]
43. Kim, S.J.; Lee, D.; Chae, J.Y.; Ko, B.; Lee, H.; Paik, T.; Hong, S.H. Reconfigurable, vivid reflective colors based on solution-processed Fabry–Perot absorber using thermochromic vanadium dioxide. *Appl. Surf. Sci.* **2021**, *565*, 150610. [CrossRef]
44. Du, Z.Y.; Li, M.; Xu, S.C.; Li, K.B.; Zou, F.X.; Zhang, R.R.; Li, G.H. VO_2-based intelligent thermal control coating for spacecraft by regulating infrared emittance. *J. Alloys Compd.* **2022**, *895*, 162679. [CrossRef]
45. Sun, K.; Riedel, C.A.; Urbani, A.; Simeoni, M.; Mengali, S.; Zalkovskij, M.; Bilenberg, B.; de Groot, C.H.; Muskens, O.L. VO_2 Thermochromic Metamaterial-Based Smart Optical Solar Reflector. *ACS Photonics* **2018**, *5*, 2280–2286. [CrossRef]
46. He, D.; Liu, Z.J.; Fernandes, G.E.; Shen, T.Y.; Oller, D.; Pacifici, D.; Kim, J.H.; Xu, J. High-purity red coloration via mode-selective absorption in a layered thin-film cavity. *Aip Adv.* **2018**, *8*, 065226. [CrossRef]
47. Palik, E.D.; Ghosh, G. *Handbook of Optical Constants of Solids*; Academic Press: San Diego, CA, USA, 1998.
48. Ke, Y.; Wen, X.; Zhao, D.; Che, R.; Xiong, Q.; Long, Y. Controllable Fabrication of Two-Dimensional Patterned VO(2) Nanoparticle, Nanodome, and Nanonet Arrays with Tunable Temperature-Dependent Localized Surface Plasmon Resonance. *ACS Nano* **2017**, *11*, 7542–7551. [CrossRef]
49. Chen, Y.-S.; Ho, H.-C.; Lai, Y.-C.; Nagao, T.; Hsueh, C.-H. Thermochromic vanadium dioxide film on textured silica substrate for smart window with enhanced visible transmittance and tunable infrared radiation. *Infrared Phys. Technol.* **2019**, *102*, 103019. [CrossRef]
50. Li, S.Y.; Niklasson, G.A.; Granqvist, C.G. Nanothermochromics: Calculations for VO_2 nanoparticles in dielectric hosts show much improved luminous transmittance and solar energy transmittance modulation. *J. Appl. Phys.* **2010**, *108*, 063525. [CrossRef]
51. Mlyuka, N.R.; Niklasson, G.A.; Granqvist, C.G. Thermochromic VO_2-based multilayer films with enhanced luminous transmittance and solar modulation. *Phys. Status Solidi (A)* **2009**, *206*, 2155–2160. [CrossRef]
52. Huang, X.; Huang, J.; Qian, Y.; Yang, L.; Zhang, Z.; Yang, J. Nonvolatile phase-change materials color display designed by evolutionary search. *Results Phys.* **2021**, *29*, 104701. [CrossRef]
53. Santos, G.; Losurdo, M.; Moreno, F.; Gutierrez, Y. Directional Scattering Switching from an All-Dielectric Phase Change Metasurface. *Nanomaterials* **2023**, *13*, 496. [CrossRef]
54. Westland, S.; Ripamonti, C.; Cheung, V. *Computational Colour Science Using MATLAB*, 2nd ed.; Wiley: Hoboken, NJ, USA, 2012; p. xii.
55. Huang, X.; Huang, J.; Yang, L.N.; Zhang, Z.F.; Ma, H.S.; Qian, Y.; Li, C.X.; Zhang, Z.R.; Yang, J.B. All-Dielectric Metasurfaces Color Filter Arrays Designed by Evolutionary Search. *IEEE Photonics J.* **2021**, *13*, 7100409. [CrossRef]
56. Zhu, Y.Q.; Tian, X.; Fang, J.K.; Shi, Y.P.; Shi, S.N.; Zhang, S.; Song, J.M.; Li, M.P.; Liu, X.Y.; Wang, X.D.; et al. Independently tunable all-dielectric synthetic multi-spectral metamaterials based on Mie resonance. *RSC Adv.* **2022**, *12*, 20765–20770. [CrossRef] [PubMed]

Disclaimer/Publisher's Note: The statements, opinions and data contained in all publications are solely those of the individual author(s) and contributor(s) and not of MDPI and/or the editor(s). MDPI and/or the editor(s) disclaim responsibility for any injury to people or property resulting from any ideas, methods, instructions or products referred to in the content.